Microstructure and phase evolution of micronized ceramic colorants from a pilot plant for inks production

Matteo Ardit [a,1], Chiara Molinari [b,*,1], Daniele Verucchi [c], Alice Tintorri [c], Michela Migliori [c], Tanya Toschi [c], Sonia Conte [b], Chiara Zanelli [b], Giuseppe Cruciani [a], Michele Dondi [b]

[a] *Physics and Earth Sciences Department, University of Ferrara, Via Saragat 1, 44122, Ferrara, Italy*
[b] *CNR-ISTEC, Institute of Science and Technology for Ceramics, Via Granarolo 64, 48018, Faenza, Italy*
[c] *INCO Industria Colori S.p.A, Via Montebonello 19/21, 41026, Pavullo, Italy*

A B S T R A C T

The advent of inkjet printing as digital decoration of ceramic materials has irreversibly modified the industrial decoration technology, imposing companies to change the colorant production process. The inkjet application requires micronized particles in the ultrafine particle size range (smaller than 1 μm). Particles size reduction of ceramic colorants is performed by a high-energy comminution process in wet-operated bead mills, affecting colorants properties. Since a deep knowledge of milling-induced microstructural changes is still lacking, the micronization effects on a set of five industrial ceramic colorants are thoughtfully investigated in this work by simulating the industrial process at a pilot plant. Particle size distribution and energy consumption are monitored during the comminution process. The compositional (including crystallite size and microstrain analysis of the main phases) and morphological variation of four ceramic pigments (yellow zircon, brown spinel, pink malayaite, and green eskolaite) and one dye (blue olivine) is investigated by XRPD (Rietveld method) and SEM analyses. The analytical approach combined with a physical/semiempirical modelling of the colorants elastic features versus the energy demand for particle reduction has yielded details on the nature of the micronization-induced microstructural changes in ceramic colorants. Specifically, the comminution efficiency as well as the crystalline phase stability are related to the intrinsic properties of each colorant. Brittle breakage rather than plastic deformation on comminution are also system dependent. When an euhedral to subhedral crystal habit is maintained a brittle fracture is preserved throughout the comminution progress, while the formation of flake-like particles and particle agglomeration are strong evidences of plastic deformation. The last evidence deals with the material elastic features. Materials with high bulk modulus convert the grinding energy to lattice defects that lead to particle breakage by brittle fractures, while materials with lower bulk modulus convert/dissipate part of the supplied energy in plastic deformations, drastically decreasing the comminution process efficiency.

1. Introduction

The comminution of solid bodies in the submicron size range is a process of interest for various industrial sectors, such as mining, pharmaceutical, food and ceramics [1]. Particles smaller than 1 μm can be obtained through bottom-up processes, i.e., through chemical synthesis methods that produce materials with high purity and specific physico-chemical properties. Nevertheless, top-down processes, such as comminution in wet-operated stirred-media mills, are a valid alternative to produce suspensions of concentrated submicrometric particles with

high performance in a relatively simple and well established process [2–4].

In the ceramic industry, inkjet printing has become the most popular, if not ubiquitous, decoration technique [5]. Although extremely versatile (because of non-contact decoration, high-quality images, printing on textured surfaces, less wastage of inks and additives, and no need of screens), inkjet printing forced colorants manufacturers to take a further step in the production chain. Indeed, the finished product is no longer a powder with median particle size d_{50} of 5–20 μm for ordinary pigments) but is an ink, where colorant is dispersed in a carrier [6]. Inkjet print

heads require colorant particle size to be reduced to achieve at least 99% of the particles below 1 μm. Therefore, in the manufacturing process, ceramic inks undergo a high-energy comminution process in wet-operated bead mills [5,6]. This additional production step helps to prevent clogging of the print head nozzles and ensures the stability of the suspension over time [7–9]. On the other hand, the protracted comminution process strongly affects colorimetric performances, mechanical properties, and resistance to amorphization of colorants with effects not yet well defined [6–13].

The comminution progress mainly depends on specific energy input, which is the total energy supplied to the grinding chamber related to the product mass. The process acting in the grinding chamber of a mill can be essentially described by the number of stress events, their intensity (stress energy), and the specific energy [14]. The effect of these parameters on the product fineness is determined by the breakage characteristics of the material and particle-particle interactions [2,3,15]. Besides specific energy, the choice of the grinding media size has a great influence on the comminution result. The specific energy consumption is further affected whether the dimension of grinding media does not properly match the size of the product particles [2, and references therein].

When producing ultrafine particles, interparticle interactions are more and more relevant, and comminution process in submicrometric size range becomes the most demanding in terms of energy per unit weight of product [1–3]. The process is strongly influenced by an increasing collision rate of the particles due to their Brownian motion and smaller interparticle distances [2,3,16–19].

Submicrometric comminution is energetically expensive and inefficient due to possible agglomeration phenomena that increase the viscosity of the suspension (high solid concentrations or strong attractive interparticle interactions that affect the suspension rheology) and reduce the grinding beads kinetics [17]. Brittle fractures, cold-welding, and plastic deformation are key factors in high-energy ball milling processes [20]. The convolution of all these aspects determines way and extent of the changing in shape and size for particles under comminution [21].

The goal of the present work is to provide a deeper understanding on the microstructural evolution of ceramic colorants under comminution in the ink-making process.

2. Materials and methods

2.1. Materials

Five commercially available ceramic colorants (four pigments and one dye) were selected on the basis of their different compositional (phase and chemistry) and colorimetric characteristics, in order to prepare oil-based inks designed to replicate typical industrial formulations. Namely, selected colorants and their main features were: Pr-doped zircon, **zrc** (a yellow pigment powder with a median particle size d_{50} = 875 nm); Zn–Fe–Cr–Al spinel, **sp** (a light brown pigment powder with d_{50} = 4197 nm); Cr-doped malayaite, **mly** (a pink pigment powder with d_{50} = 731 nm); eskolaite, **esk** (a green pigment powder with d_{50} = 2500 nm); and cobalt olivine, **ol** (a blue dye powder with d_{50} = 840 nm). Prior the comminution process, the colorant powders were admixed with fatty acid ethers in variable proportions based on the specific ink to be obtained (i.e., the solid load was 35% of colorant powder for **ol**, 40% for **sp** and **esk**, and 45% for **zrc** and **mly**). A table with the main physical properties (i.e., cleavage, fracture, density, Mohs hardness, Vickers hardness, fracture toughness, bulk modulus, elastic modulus, and Poisson coefficient) for each ceramic colorant is reported as supplementary material (Table S1).

2.2. Comminution setup and procedure

The micronization process was carried out at the INCO Spa ceramic

colorants factory, where 2 kg of ink for each ceramic colorant were comminuted in a pilot plant to simulate the industrial process. Inks comminution was carried out by a I-MILL 0.5 circulation type agitator bead mill (i-TECH srl) using spheres (mean diameter of 300 μm) of Y-stabilized tetragonal zirconia as grinding media. Although characterized by a different starting particle size, the comminution process was rationalized so that all colorants underwent a particle size reduction down to approximately 270 nm range, i.e., below the industrial target for inkjet decoration. In detail, a first aliquot of each sample under comminution was taken from the milling chamber when $d_{50} \approx 590$ nm. Further three aliquots of ink were collected from the milling chamber at increasing time for $d_{50} \approx 400, 350$ and 270 nm. Particle size distribution was measured by laser diffraction (Fritsch-Analysette 22) directly on the ink. Precision and accuracy of laser diffraction measurements comply with the international standard ISO 13320 "Particle Size Analysis – Laser Diffraction Methods" where d_{50} values deviate less than 3% from those obtained with a Standard Reference Material, while d_{10} and d_{90} values deviate less than 5%. Time of comminution and energy consumption were collected by bead mill software throughout the micronization process (Table 1). Energy consumption (E_c) was calculated starting from the first aliquot picking of the sample and normalized for the colorant solid load.

2.3. Powder characterization

The organic fraction was removed from the micronized products by thermal treatment at 500 °C (heating rate 50 °C·h^{-1}). The absence of combustion residues was verified by simultaneous thermo-gravimetric and thermo-differential analysis (TG/DTA, 5 °C·min^{-1} up to 800 °C in a flux of air at 20 ml min^{-1}). The ceramic colorants microstructure was observed by a scanning electron microscope (FEG-SEM, Zeiss, Sigma) with a magnification range between 15 and 100 X. Specimens were sputtered coated with gold, and pictures were collected using secondary electrons. Specific surface area measurement for each sample was performed through the BET method with a FlowSorb 2300 analyzer (Micromeritics Instrument, USA). Helium was used as absorbed gas.

Table 1
Inks comminution details. Sample label, solid load to liquid ratio (SLR), comminution time (t), energy consumed (E_c) and particle size diameters (d_{50}, d_{90}, and d_{99}).

label	SLR (%)	time, t (min)	energy, E_c (kWh·kg^{-1})	d_{50} (nm)	d_{90} (nm)	d_{99} (nm)
yellow zircon (zrc)						
zrc590	45/55	0	0.00	590	1412	2332
zrc400		45	0.40	413	1.057	1957
zrc350		70	0.62	354	854	1626
zrc270		130	1.11	273	571	1335
pink malayaite (mly)						
mly590	45/55	0	0.00	603	1748	2370
mly400		40	0.21	402	1161	1616
mly350		72	0.64	344	1019	1497
mly270		157	1.94	268	906	1489
brown spinel (sp)						
sp590	40/60	0	0.00	593	1691	2290
sp400		42	0.33	402	1195	1772
sp350		65	0.44	351	1058	1704
sp270		137	1.00	272	626	1481
green eskolaite (esk)						
esk590	40/60	0	0.00	592	1842	2457
esk400		11	0.11	413	1293	1760
esk350		26	0.50	357	1064	1541
esk270		105	0.99	264	512	674
blue olivine (ol)						
ol590	35/65	0	0.00	590	1401	2298
ol400		50	0.57	393	820	1413
ol350		90	1.00	352	907	1829
ol270		180	2.14	272	599	1539

2.4. X-ray powder diffraction (QPA-XRPD) measurements

Prior to XRPD measurements, each sample was admixed with 15 wt % corundum (NIST alumina powder SRM 676) as internal standard for the quantification of the crystalline phases and XRD amorphous content [22,23]. Data collection was performed on a D8 Advance Da Vinci diffractometer (Bruker, Karlsruhe, Germany) working in Bragg-Brentano geometry, and equipped with a Cu-anode X-ray tube, Ni-filter to suppress the $CuK\beta$ component, and a LynxEye XE silicon strip detector ($2.585°$ of window size) set to discriminate the $CuK\alpha_{1,2}$ radiation. The powder of each sample was scanned in a continuous mode from 5 to 90° 2θ, with step size of 0.02° 2θ and a counting time of 1 s per step. In order to minimize crystallites preferred orientation and increase the counting statistics, the sample was spun at 25 rpm, and a knife perpendicular to the sample was placed at a suitable distance from the sample surface to reduce the air-induced scattering. A cascade plot, where collected diffraction patterns for each ceramic colorant are compared at each comminution step, is reported as supplementary material (Figs. S1–S5).

2.5. Phase identification and Rietveld refinement

Qualitative phase analysis was performed by means of the EVA software v.6.0 (Bruker). Collected XRPD patterns were modeled by means of the fundamental-parameter Rietveld approach (TOPAS v.5.0, Bruker). As the certified value of crystalline corundum SRM 676 was 91.75(1.52) wt%, a 13.76 wt% corundum fraction was kept fixed during the refinement procedure as spiked phase. All the identified phases were modeled by carrying out multiphase refinements in which only the scale factors, the unit-cell parameters, and the crystallite size and strain were varied. Crystallite size and microstrain were calculated by means of the "integral breadth" algorithm as derived from a profile peak convolution in a Lorentzian-type broadening approximation. Known instrumental parameters (e.g., goniometer radius, slit sizes, geometrical parameters of the X-ray tube, etc.) were used to calculate the instrumental contribution to the peak profiles, the zero-error correction was fixed at the value determined using the NIST Si standard (SRM 640e), and refinements included a specimen displacement correction and a Chebyshev polynomial curve to model the background. Rietveld refinement plots for all the investigated samples are reported as supplementary material (Figs. S6–S10). Refinement agreement factor R_{wp}, quantitative phase analysis, and crystallite size (x_{XRD}) and microstrain (e_0) of the main phase are reported in Table 2.

3. Results

3.1. Particle size dependence on comminution time and energy

Fig. 1 shows the amount of energy consumed (E_c) in relation to the time (t) taken to reduce the ink particles from a d_{50} of 590 to 270 nm. E_c and t are clearly correlated with characteristic trends that depend on the intrinsic properties of each ink. With the only exception of *mly*, the time spent for the comminution of *zrc*, *sp*, *esk* and *ol* colorants shows well defined linear trends with the energy consumed. The energy required to reduce the particle size of colorants to the ultrafine range ($d_{50} < 1$ μm) ranges from about 1 kWh·kg^{-1} for *esk*, *sp* and *zrc* up to about 2 kWh·kg^{-1} for *mly* and *ol*. Similarly to the trend defined by E_c, the comminution time ranges from 105 min for *esk*, to about 130 min for *zrc* and *sp*, up to times greater than 150 min for *mly* and *ol* (157 and 180 min, respectively).

Table 2

Refinement agreement factor (R_{wp}), space group (*s.g.*), quantitative phase analysis (crystalline and amorphous phases), and crystallite size (x_{XRD}) and microstrain (e_0) of the main phase for comminuted ceramic colorants.

| label	R_{wp}(%)	crystalline phases (wt%)					amorphous (wt%)	crystallite size, x_{XRD} (nm)	microstrain $e_0 \times 100$
yellow zircon (zrc)									
		zircon	quartz	baddeleyite				zircon	
s.g.		$I4_1/amd$	$P3_221$	$P2_1/c$					
zrc590	6.51	78.7(7)	9.0(2)	4.2(1)			8.1(7)	139(5)	0.098(1)
zrc400	6.66	77.2(7)	8.2(2)	4.3(1)			10.2(7)	96(3)	0.111(1)
zrc350	6.45	77.6(7)	8.0(2)	4.8(1)			9.6(7)	88(3)	0.119(1)
zrc270	6.28	76.5(7)	7.6(2)	5.6(1)			10.2(7)	60(1)	0.121(2)
pink malayaite (mly)									
		malayaite	uvarovite	wollastonite	cassiterite	quartz		malayaite	
s.g.		$C2/c$	Ia-$3d$	P-1	$P4_2/mnm$	$P3_221$			
mly590	6.22	70.6(7)	5.7(1)	3.3(1)	2.8(1)	1.2(1)	16.4(7)	65(2)	0.068(2)
mly400	5.55	65.3(6)	5.4(1)	2.9(1)	2.4(1)	1.2(1)	22.9(6)	40(1)	0.084(3)
mly350	6.18	63.8(6)	5.1(1)	3.2(1)	2.0(1)	0.9(1)	24.9(7)	35(1)	0.103(4)
mly270	5.91	60.6(6)	4.5(1)	2.6(1)	1.6(1)	1.1(1)	29.7(7)	24(1)	0.122(5)
brown spinel (sp)									
		spinel-1	spinel-2	quartz	zincite			spinel-1	
s.g.		Fd-$3m$	Fd-$3m$	$P3_221$	$P6_3mc$				
sp590	7.20	76.4(6)	15.0(1)	2.6(1)	0.3(1)		5.7(6)	114(5)	0.154(3)
sp400	6.70	75.5(5)	14.9(1)	2.4(1)	0.4(1)		6.9(5)	72(3)	0.186(4)
sp350	6.56	76.5(5)	15.1(1)	2.5(1)	0.3(1)		5.6(5)	59(2)	0.200(4)
sp270	6.49	75.4(4)	14.9(1)	2.7(1)	0.3(1)		6.7(5)	45(2)	0.228(5)
green eskolaite (esk)									
		eskolaite	zirconia					eskolaite	
s.g.		R-$3c$	$P4_2/nmc$						
esk590	8.38	94.5(7)	1.3(1)				4.3(6)	164(4)	0.018(1)
esk400	8.50	92.2(7)	1.7(1)				6.1(6)	144(4)	0.020(1)
esk350	8.78	89.9(7)	2.7(1)				7.4(6)	122(3)	0.023(1)
esk270	9.13	79.4(7)	6.2(1)				14.4(7)	82(2)	0.041(1)
blue olivine (ol)									
		olivine	cristobalite	quartz				olivine	
s.g.		$Pnma$	$P4_12_12$	$P3_221$					
ol590	2.52	73.1(10)	6.3(1)	7.5(1)			13.1(10)	78(6)	0.088(4)
ol400	2.42	71.2(10)	4.7(1)	5.9(1)			18.3(9)	49(3)	0.104(5)
ol350	2.40	73.0(10)	4.4(1)	5.9(1)			16.8(9)	41(2)	0.112(6)
ol270	2.38	73.3(11)	3.7(1)	5.4(1)			17.6(12)	30(1)	0.113(7)
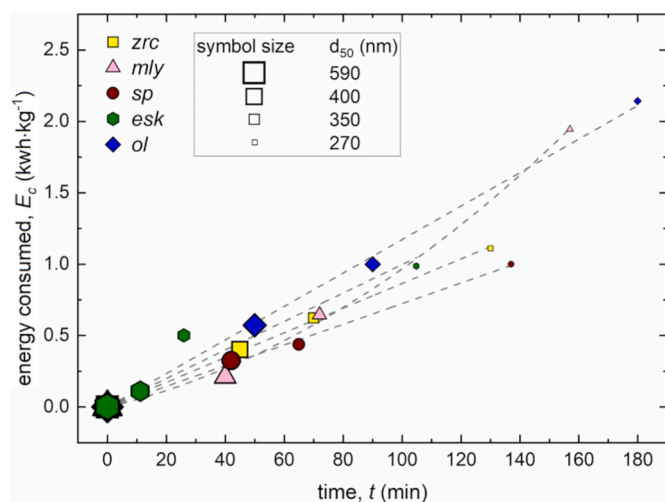
Fig. 1. Time (t) and energy consumed (E_c) dependence for ceramic inks comminuted in the $590 > d_{50} > 270$ nm. Symbol sizes exceed the estimated uncertainties in measurements. Dashed lines are a reader's eye guide.

3.2. Phase composition

All investigated samples are polyphasic except for *esk*. The latter, monophasic at the beginning of the comminution process, is characterized by a small amount of Y-stabilized tetragonal zirconia which increases at the highest values of milling time and energy (Table 2). Such an enhanced grinding media abrasion is likely caused by eskolaite being the hardest colorant between those under investigation.

Besides causing variations in the crystalline phases fraction, the comminution process variably affects the amount of the amorphous phase (Table 2). Fig. 2 shows the variation of the amorphous content for the investigated ceramic colorants at different comminution steps (from $d_{50} \approx 590$ nm downward) as a function of E_c.

In detail, *sp* exhibits a tiny increase in the amorphous phase content (from 5.7 to 6.7 wt%) corresponding to a decreasing of the spinel main phase. In fact, the phase fraction of further components does not change during the comminution process. Along with a second phase with spinel structure, quartz and zincite are identified as unreacted precursors from the *sp* pigment synthesis. Also, *zrc* shows a modest increase in the amorphous phase content (from 8.1 to 10.2 wt%) as a function of E_c (and
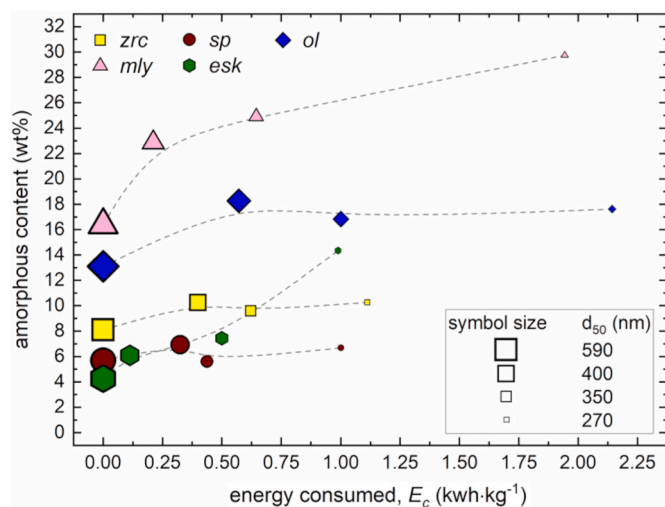
t, Table 2 and Fig. 2). This variation seems to match the gradual decrease of zircon and quartz, and an increase in baddeleyite (monoclinic ZrO_2 form). Both quartz and baddeleyite are unreacted precursors usually found after the *zrc* pigment synthesis [8,24,25]. The degree of amorphization for samples *mly* and *esk* is quite different from that of *zrc* and *sp* (Table 2). Along with malayaite as the main phase, *mly* is characterized by several secondary phases, either unreacted precursors (cassiterite and quartz) and undesired products (uvarovite and wollastonite) of the pigment synthesis. For this sample, the degree of amorphization does not change gradually during the comminution process. Indeed, *mly* exhibits a drop of malayaite phase fraction in the first comminution step ($603 > d_{50} > 402$ nm) where the amorphous content steeply raises from 16.4 to 22.9 wt% (Fig. 2). Hereafter, the sample amorphization is more gradual until the end of the comminution process, when the amorphous phase reaches almost 30 wt% (3.3 wt% from the secondary phases). Otherwise, the sample *esk* is characterized first by a gradual eskolaite content decreasing down to $d_{50} \approx 360$ nm (corresponding to amorphous phase from 4.3 to 7.4 wt%) then by a steep amorphization in the last comminution step, where the amorphous phase reaches 14.4 wt%. Such an increase is not fully balanced by the loss of pigment (-15.0 wt% eskolaite vs. $+10.1$ wt% amorphous phase) because of the increasing of Y-stabilized zirconia phase fraction during the comminution process, which alters the original formulation (Table 2).

Although the amorphization pathway displayed by the sample *ol* is like that of *zrc* and *sp* (Fig. 2), the comminution effects on the constituent phases are different from those described for the previous samples. The amorphous phase content increases in the first comminution step (from 13.1 to 18.3 wt%) then levels around a constant value of about 17.5 wt %. At variance with the ceramic pigments, the olivine phase fraction (i. e., *ol* main phase) is almost unaffected during the comminution process. Conversely, a moderate decreasing of cristobalite and quartz (unreacted precursors) is observed (Table 2).

3.3. Unit-cell parameters of colorants main phase

The unit-cell parameters of the main phases for each colorant are listed in Table 3.

All these phases display tiny volumetric variations (few hundredths of a percentage point), with eskolaite and malayaite having the minimum ($\delta V \approx 0.01\%$) and maximum ($\delta V \approx 0.05\%$) volumetric variation, respectively (Fig. S11). In some specific cases (i.e., malayaite, zircon, and to a less extent olivine), the variation of the lattice parameters seems to define trends where the unit-cell volume as well as lattice parameters increase (zircon) or decrease (malayaite and olivine). Given the subtle nature of these variations, relating these apparent trends to the crystal structure or other physical properties of the different colorants is not straightforward. In the literature, the size-dependence of surface free energy of particles has been invoked for anatase nanocrystals to explain the contraction of the unit-cell dimensions with decreasing particle size in the 5–35 nm range [26]. The integration of the surface stress calculated from the lattice contraction and the bulk modulus of materials, was used to derive the surface free energy of nanocrystalline anatase [26]. It was concluded that two opposing factors contribute to the variation of the surface energy with the particle size: the increase of surface free energy with decreasing particle size due to presence of more high-energy sites, and the decrease of surface free energy due to closer structural correspondence between surfaces and interiors of nanoparticles as the particle size decreases [26]. We speculate that the prevalence of the two opposing factors might be not only size-dependent but also crystal structure-dependent. It can be further considered that the absence of chains of octahedra in zircon, contrary to malayaite, olivine and anatase, would be consistent with the different behavior of the former. It must be pointed out, however, that the unit-cell variations we have found are very subtle and occur within a range of much larger particle size than in nanoanatase [26]. Therefore, we cannot rule out that the variation of

Fig. 2. Variation of the colorant amorphous content as a function of the energy consumed, E_c. Error bars are within the symbol size. Dashed lines are a reader's eye guide.

Table 3
Refined unit-cell parameters of the main phase for comminuted ceramic colorants.

	label	unit-cell parameters				
zircon (s.g. $I4_1/amd$)		a (Å)	b (Å)	c (Å)	β (°)	V (Å^3)
	zrc590	6.6196(1)		5.9917(1)		262.55(1)
	zrc400	6.6197(1)		5.9920(1)		262.57(1)
	zrc350	6.6199(1)		5.9921(1)		262.59(1)
	zrc270	6.6201(1)		5.9925(2)		262.62(1)
malayaite (s.g. $C2/c$)						
	mly590	7.1441(2)	8.8875(2)	6.6617(2)	113.33(1)	388.40(2)
	mly400	7.1435(2)	8.8871(3)	6.6602(3)	113.31(1)	388.31(3)
	mly350	7.1434(3)	8.8873(4)	6.6597(3)	113.32(1)	388.26(4)
	mly270	7.1432(4)	8.8870(6)	6.6579(4)	113.30(1)	388.20(5)
spinel (s.g. Fd-$3m$)						
	sp590	8.2303(1)				557.50(3)
	sp400	8.2304(2)				557.51(4)
	sp350	8.2304(2)				557.53(4)
	sp270	8.2297(3)				557.39(7)
eskolaite (s.g. R-$3c$)						
	esk590	4.9587(1)		13.5959(1)		289.52(1)
	esk400	4.9587(1)		13.5960(1)		289.52(1)
	esk350	4.9588(1)		13.5964(2)		289.54(1)
	esk270	4.9589(1)		13.5967(3)		289.55(1)
olivine (s.g. $Pnma$)						
	ol590	10.3040(5)	6.0032(3)	4.7828(3)		295.85(3)
	ol400	10.3052(7)	6.0022(4)	4.7828(4)		295.84(4)
	ol350	10.3053(8)	6.0021(4)	4.7826(4)		295.82(4)
	ol270	10.3041(10)	6.0008(5)	4.7837(5)		295.79(5)

lattice parameters we observed for the colorant main phases are merely explained by the larger uncertainty on the peak positions determined by the Rietveld fit due to the increased broadening of diffraction peaks related to the decrease of crystallite average size with the ongoing comminution process (Figs. S1–S5).

3.4. Specific surface area

The formation of a new specific surface area (SSA) increases proportionally (along sublinear trends except for *esk*) with E_c during the comminution process (Fig. 3a).

Sp, *zrc*, and *mly* display subparallel trends, indicating that the rate of formation of new SSA is very similar for these colorants. The rate of formation of new SSA for *ol* is slower (it requires more energy per unit SSA produced). This may be ascribed to the behavior of the dye constituent phases during the comminution process beyond what reported, i.e., the olivine phase fraction remains unchanged during the comminution process, while the secondary phases cristobalite and quartz undergo a gradual fraction decreasing. The non-linear trend of *esk* is

consistent with the largest decrease of crystallite size measured by XRD for this colorant after the last grinding step.

As shown in Fig. 3b, the size of particles, as derived from BET measurements (x_{BET}) — calculated through the mass-SSA relationship under the assumption of spherical and monodisperse particles with a bulk density, ρ_p ($x_{BET} = \frac{6}{\rho_p \cdot SSA}$) — is much smaller than that obtained from laser diffraction measurements (the median particle size, d_{50}). As suggested by Knieke et al. [17], this could indicate that colorant particles form agglomerates caused by unstable suspension conditions which cannot be detected by BET.

3.5. Microstructural features of colorants

SEM microstructures of the starting samples are reported in Fig. 4. A main difference can be observed, that clearly reflects previous steps of the production process. In case of *sp* and *esk*, the starting powders exhibit some particles (reaching a size up to 2 μm) with morphology typical of spinel (octahedral habit) or eskolaite (pyramids, and barrel-shaped crystals with a short prism and a large base). In addition, for *esk*, a
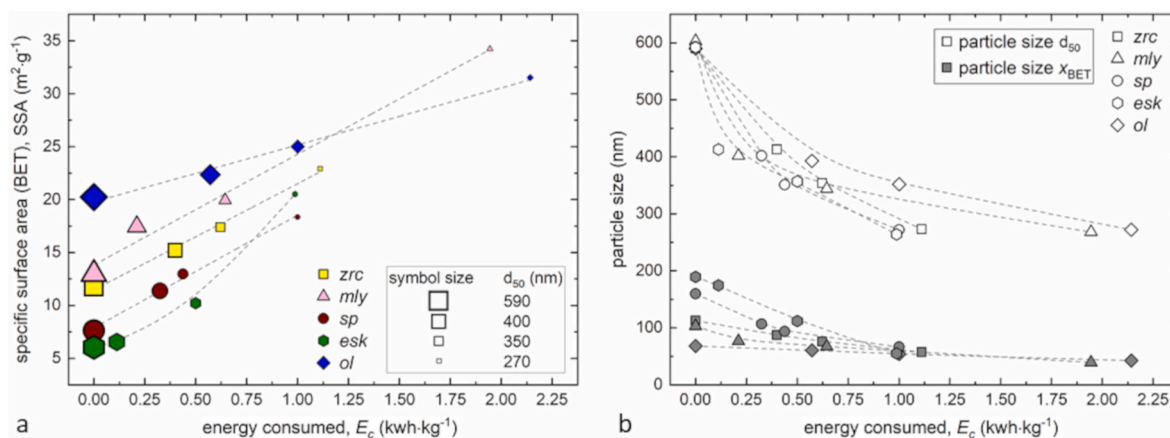

Fig. 3. Variation of colorants specific surface area (BET), SSA (*a*), and particle size (both from BET and laser diffraction in *b*) as a function of the energy consumed, E_c. Error bars are within the symbol size. Dashed lines are a reader's eye guide.
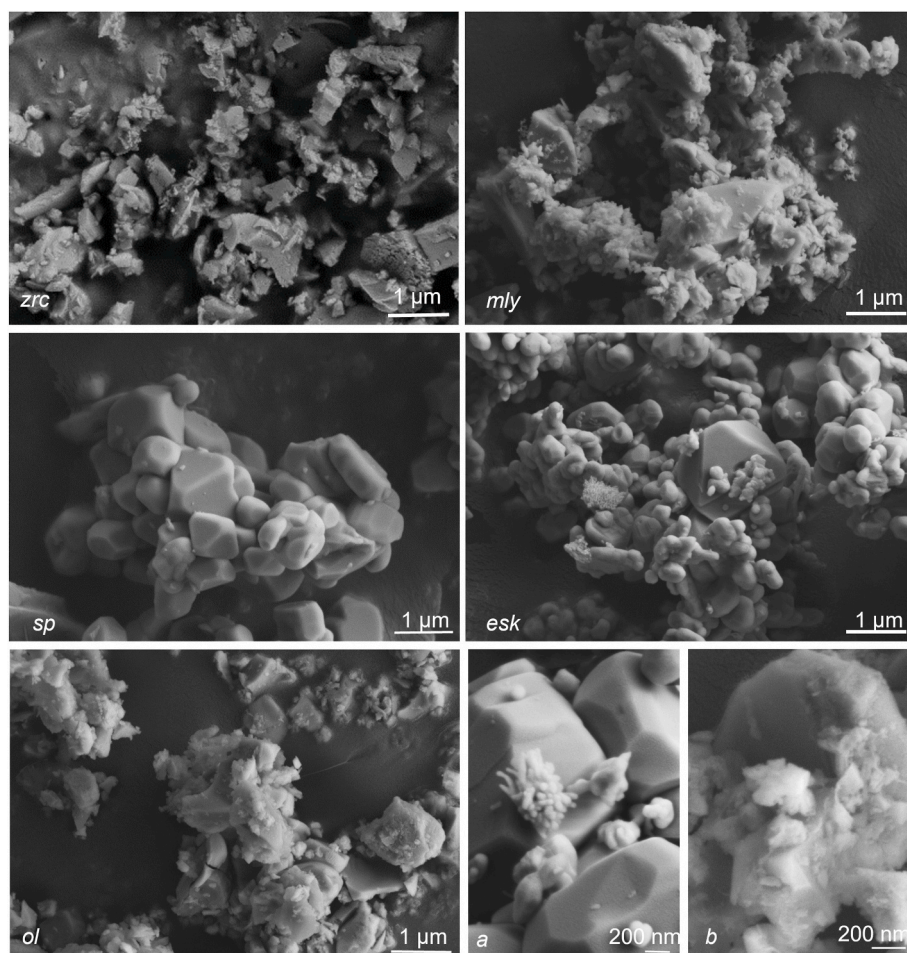
Fig. 4. Starting sample microstructures; *a* and *b* refer to high magnification details for *esk* and *ol* samples, respectively.

strong bimodal particle size distribution can be observed, analogously to *zrc*, *ml* and *ol*. For the latest three, together with the bigger particles with dimension of about 1 μm, the presence of small fragments of 0.2 μm or so can be noted. In all cases, particles show morphologies proper of brittle fracture, deriving from a post-synthesis milling step, and suggesting different breakage mechanisms as a function of the crystal structure.
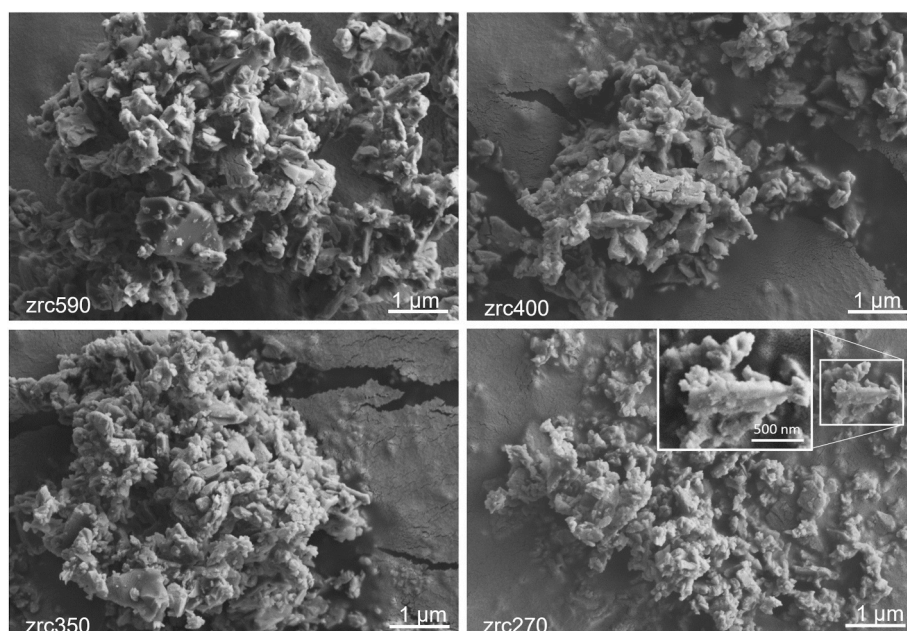

Fig. 5. *Zrc* microstructure evolution as a function of comminution progress.

Indeed, *zrc* exhibits irregular particles with sharp edges (square prismatic crystals), suggesting a non-preferential propagation of cracks (poor cleavage). The original zircon habit is rarely observed. Otherwise, *mly* shows some malayaite particles with typical wedge-shaped morphology based on pinacoids (good cleavage on {110}) together with irregular fragments characterized by conchoidal fracture. In the case of *ol*, euhedral to subhedral olivine crystals are observed, with cleavage on {010}.

The particle size reduction is followed by a microstructural evolution, which defines different pathways, like brittle fracture (according to cleavage or irregular fragmentation) and plastic deformation (including particle agglomeration).

For *zrc* sample, a brittle fracture mechanism dominates in the early comminution stages (Fig. 5). In case of *zrc*590, irregular particles and cracked fragments can be easily observed. The bimodal size distribution of the starting pigment is partially maintained, since both particles coarser than 1 µ and those milling-derived can be seen. Further size reduction (late comminution steps) reduces the polydispersity and leads to anhedral particles (from coarse-granular to compact), stemming from both particle agglomeration and plastic deformation.

These latest mechanisms determine the formation of particles coarser than the nominal values determined by laser diffraction. This effect is especially evident for *mly*, where the formation of flake-like particles is observed at every comminution step (Fig. 6). Particles agglomeration in *mly* induces to a higher size and morphology homogeneity.

A different microstructural evolution with comminution is observed for the *sp* sample (Fig. 7). A strong bimodal size distribution is maintained for *sp*590, with the co-presence of main particles (coarser than 1 µm) and milling-derived fragments (finer than 300 µm). As the comminution process progresses, the particle size reduction is accompanied by the formation of well-defined subhedral elements, that clearly derive from a brittle comminution mechanism, likely due to parting of octahedral crystals along the separation plane {111}.

The brittle fracture mechanism becomes particularly evident in case of *esk* (Fig. 8). For *esk*590, the size polydispersity of the starting material is maintained. In particular, particles coarser than 1 µm with typical eskolaite habit (barrel-shaped crystals) can be clearly recognized. The progressive milling leads to a more homogeneous particle size distribution, even if a distinctive morphology is preserved until the end of the

comminution process, hence suggesting a predominant mechanism acting through a regular crystal parting.

The *ol* sample shows a trend similar to that of *zrc* and *mly* (Fig. 9). For this dye, the formation of subhedral flattened particles is more pronounced. Also in this case, the starting particle size polydispersity is gradually reduced. The presence of aggregates bigger than the nominal particle size is observed in every collected micrograph.

As discussed in detail below, whether a transition from brittle to plastic deformation regime occurs in the colorants main phase cannot be inferred from the variation of the crystallite size and microstrain. On the other hand, scanning electron micrographs for each sample clearly highlight a partial plastic deformation during the comminution process, suggesting that this deformation regime occurs at non-crystalline fraction (or XRD amorphous) expense (Fig. 10).

4. Discussion

It is well known that the kinetics governing the particle breakage as well as their grinding limit depend on many variables [1,6,14–17]. Since the process parameters (e.g., rotational speed of the stirrer) and equipment (grinding media size and material, same milling apparatus) were kept constant during the experiments, other variables related to the ground materials must be considered. Indeed, the investigated inks represent complex polyphasic systems as far as the interplay between the crystalline and the amorphous/non-crystalline content in suspension with fatty acid ethers is concerned. This scenario is further complicated whether interactions among particles with different crystal structure are taken in consideration. On the other hand, the phase composition analysis revealed that only a small amount of secondary crystalline phases occurs as either unreacted precursors or unwanted synthesis byproducts (Table 2). The colorant is always the predominant phase, with the worst case represented by *mly* with 65 wt% averaged throughout the comminution process. The other samples are characterized by a colorant fraction always higher than *mly*, on average 78, 76, 89 and 73 wt% for *zrc*, *sp*, *esk*, and *ol*, respectively (Table 2).

The particle size obtained from BET measurements (x_{BET}) for *zrc*, *mly*, *sp*, *esk* and *ol* (polyphasic) samples is close to that obtained via XRD for the crystallite size (x_{XRD}) of (single phase) zircon, malayaite, spinel, eskolaite and olivine (Table 2 and Fig. 11).

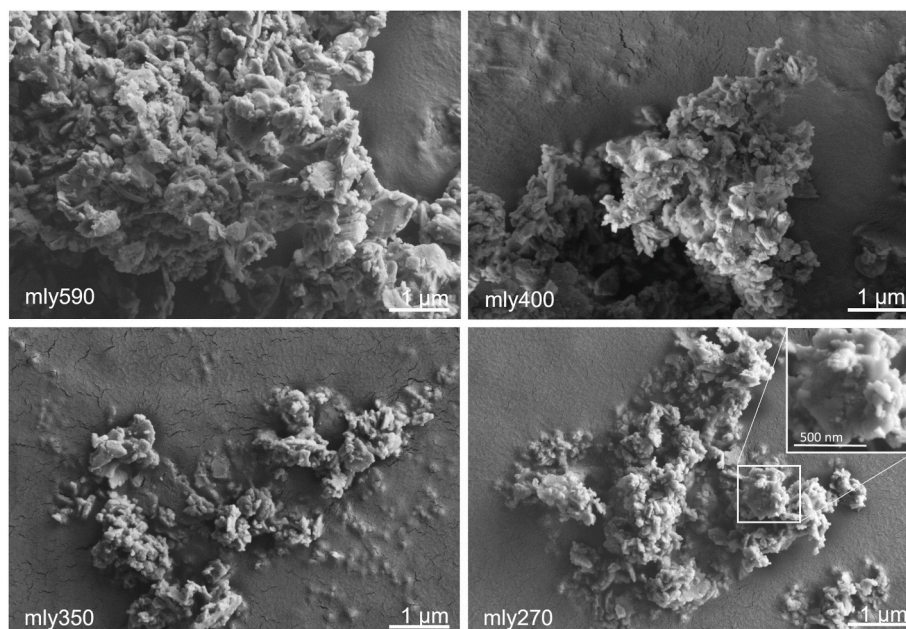The good correspondence between the XRD and BET crystallite/

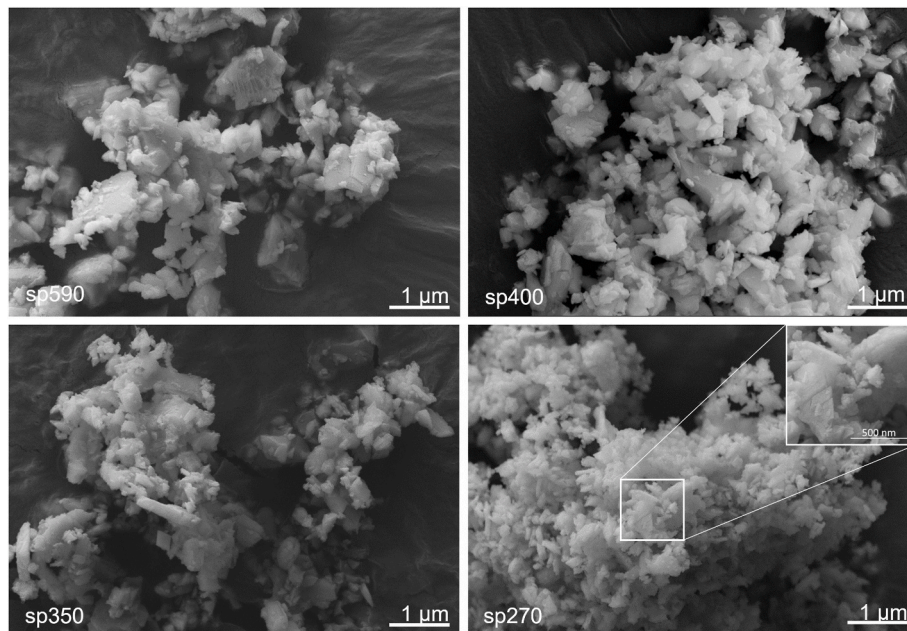**Fig. 6.** *Mly* microstructure evolution as a function of comminution progress.

Fig. 7. *Sp* microstructure evolution as a function of comminution progress.
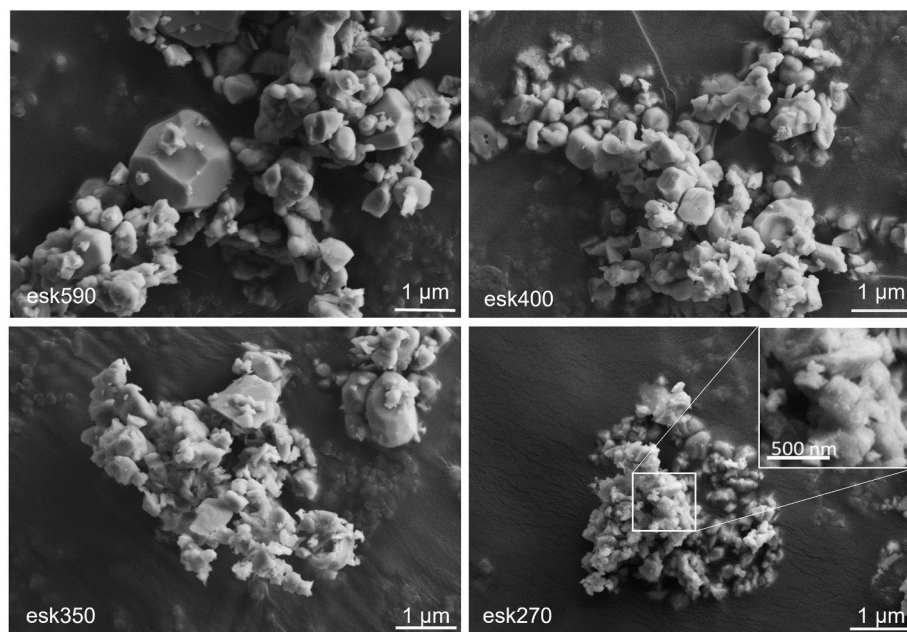

Fig. 8. *Esk* microstructure evolution as a function of comminution progress.

particle size suggests that agglomeration of particles was very limited during the comminution process. Therefore, it can be assumed that the microstructural properties of crystallites instead of the agglomerates play the most significant role during the process. As previously highlighted for other systems, when x_{BET} is close to x_{XRD}, the particle size in the milled suspension is only determined by real particle breakage [17–19]. Under the assumption that particle breakage preferentially occurs at domain interfaces or at the grain boundaries (the weakest points in a polycrystalline material), many information on the breakage process can be inferred from the energy (and time) dependence of the crystallite size (x_{XRD}; size of coherent scattering domains from the broadening effects derived by dislocation arrays, stacking faults, twins, or other extended imperfections) and the microstrain (e_0; broadening effect which can derive from dislocations or interstitial, substitutional,

and other similar point defects) as determined by XRD analysis [27].

As expected from the evolution of powder diffraction patterns collected at different comminution steps (Figs. S1–S5), where diffraction peaks for the colorants main phases show a progressive broadening, a crystallite size decreasing coupled with an enhanced strain of lattice domains is observed with increasing energy consumed (Fig. 12).

Trends defined by crystallite size values with E_c (Fig. 12a) suggest that colorants are still far away from their *true grinding limit* [17]. At variance with other investigations on particles comminution in the ultrafine range [17–19], where a plateau for $x_{XRD} \leq 10$ nm is observed, x_{XRD} values for the colorants decrease with different rates (eskolaite, zircon, spinel, olivine, and malayaite for decreasing slopes). Still, these trends suggest a potential further size reduction even for olivine and malayaite, where x_{XRD} decreased down to 30 and 24 nm, respectively
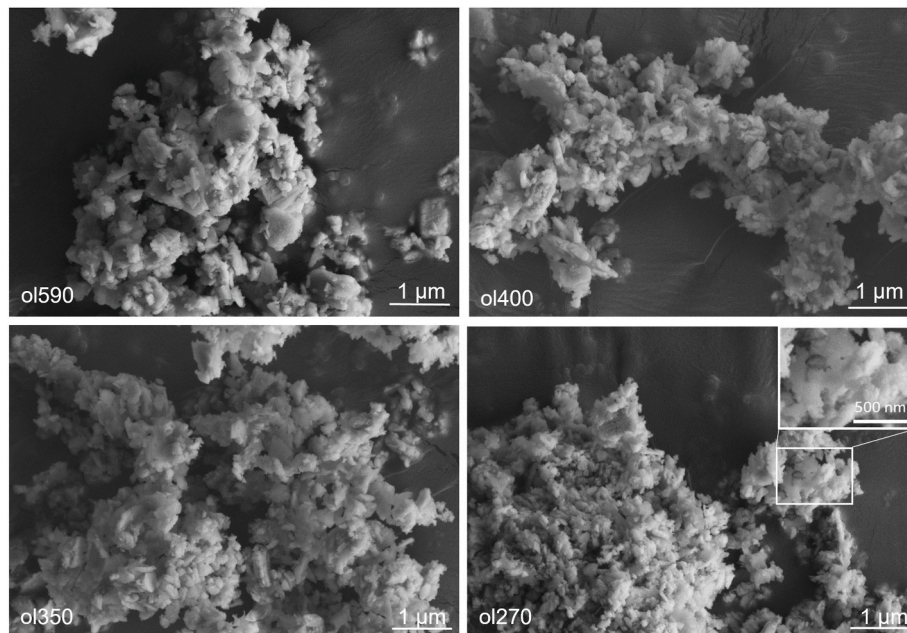
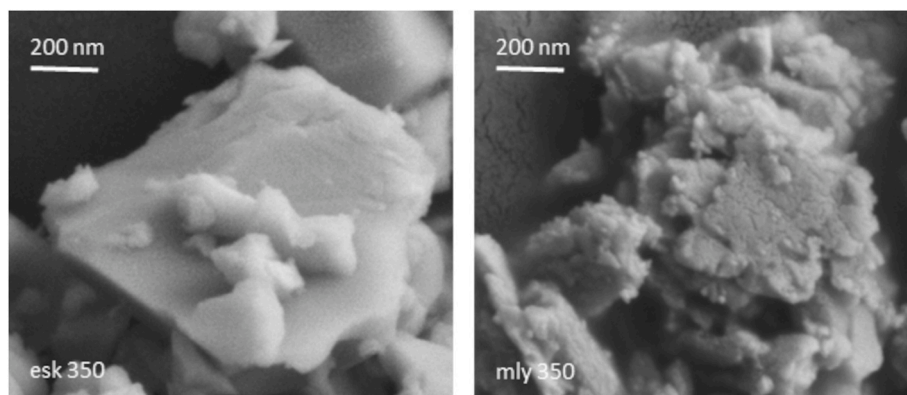**Fig. 9.** *Ol* microstructure evolution as a function of comminution progress.

Fig. 10. Comparison between brittle and plastic deformation derived microstructures.
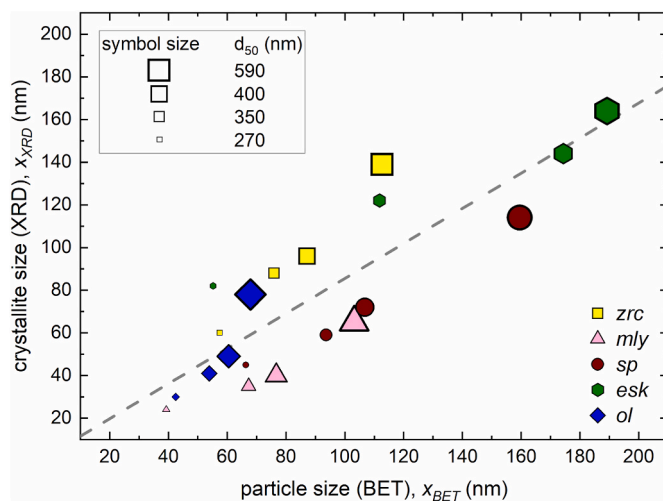

Fig. 11. Size dependence of colorants particles (by BET measurements) and crystallites (by X-ray diffraction). Dashed line is a data linear regression. Error bars are within the symbol size.

(Table 2). The comminution of ceramic inks at industrial level is not intended to reach the *true grinding limit* of the colorants, of course. However, how far the industrial process is from the minimal achievable particle size in micronization conditions [17] can be assessed by inspecting the evolution of microstrain (e_0) versus E_c (Fig. 12*b*). The *true grinding limit* would be reached if, after an increasing until a maximum value, the microstrain would drop to nearly zero. In this circumstance, the particles strength would be so high that the required elastic energy for their fracture can no longer be provided by high-energy ball milling (i.e., this is case of defect-free particles where the lattice domains are so small that no defects can be stored anymore), and the microstrain decreases [17,18,28]. In the case of the ceramic colorants, microstrain e_0 increases steeply until $d_{50} \approx 350$ nm for each main phase. Then, it grows slower for eskolaite, malayaite and spinel, while it reaches a constant value for zircon and olivine (Fig. 12*b*). In any cases, the drop of e_0 is not detected.

Our results clearly indicate that the investigated ceramic colorants can withstand a prolongation of the comminution process, meaning that the grinding media are still able to transfer enough stress intensity to induce a brittle fracture and reduce the particle size of the colorant.

It was suggested that the breakage behavior of a certain material has its own kinetics that leads to a certain grinding limit. The breakage
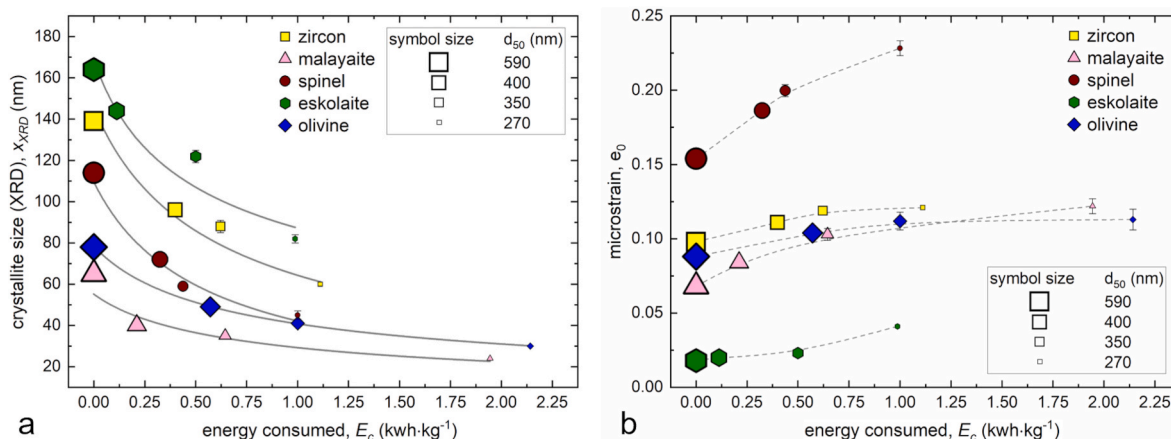
Fig. 12. Energy consumed vs. crystallite size (*a*) and microstrain (*b*) of the main phase by XRD. Curvilinear trends in Fig. *a* are a data fitting to the equation $x_{XRD} = a \cdot E_c^b$ (a detailed discussion is given below). Dashed lines in Fig. *b* are a reader's eye guide.

Table 4
Fitting parameters (*a* and *b*) and agreement index (R^2) from the E_c–x_{XRD} data fitting to Equation (2), and isothermal bulk modulus (K_{T0}), along with its range of variation, for the crystal structures of colorants under comparison.

structure type	a (nm/kWh·kg^{-1})	b	R^2	average K_{T0} (GPa)	K_{T0} range (GPa)	reference
eskolaite	94(7)	−0.39(7)	0.93	239	220–259	[31–36]
zircon	81(3)	−0.66(7)	0.97	223	205–228	[37–42]
spinel	57(3)	−0.82(10)	0.96	176	166–183	[43–45]
olivine	48(1)	−0.50(1)	0.99	144	–	[46]
malayaite	34(3)	−0.49(14)	0.87	121	–	[47]

behavior is strictly related to the degree of brittleness/ductility of the material [6,17]. It was also reported that the kinetics of crystallite breakage with energy can be approximated by a power law function, as:

$$y = a \cdot x^b \tag{Eq. 1}$$

By this way, the relative rates of change of two variables of a system are related by a pre-exponential factor (*a*) and a dimensionless exponent (*b*). Hence, this function would be able to measure the tendency to adjustment between interdependent variables. As shown in Fig. 12*a*, the rate of change of the crystallite size can be related to the rate of change of energy consumed through the following power function:

$$x_{XRD} = a \cdot E_c^b \tag{Eq. 2}$$

where the decreasing rate of x_{XRD} reduction with increasing E_C is a negative function in which the exponent is always $0 < b < 1$ and the pre-exponential factor *a* is expressed in nm/kWh·kg^{-1}. Fitting parameters and agreement factor from data fitting to Equation (2) are reported in Table 4.

As stated before, the breakage of a particle is strictly related to: i) the amount of elastic energy that grinding media can transfer; ii) the elastic properties of the particle itself; iii) the elastic properties of the grinding media. A particle with a brittle behavior can easily transfer the elastic energy coming from collision with grinding media to create lattice defects, which can lead to its breakage. On the other hand, a particle with a ductile behavior tends to dissipate the elastic energy from the grinding media (e.g., through plastic deformation). Lattice defects have a low probability to be generated; hence the particle will have low breakage probability. An attempt to explain the cause of breakage in ceramic colorants under comminution was recently reported by Molinari et al. [6]. The aptitude of particles of a given material to break during a comminution process was related to the resistance of the crystal structure to an external compression, defined by its isothermal bulk modulus (K_{T0}), which is also a measure of the resistance of a material against elastic deformation [29,30]. Isothermal bulk moduli for the crystal

structures of colorants here investigated are summarized in Table 4. The listed K_{T0} values are the average of several literature data [31–47]. For sake of clarity, the range of variation of K_{T0} is also reported in Table 4. A direct correlation between energy demand and material elastic features is difficult, because of a superposition of material and process parameters, both influencing the breakage behavior. It must be noted that the intrinsic elastic features of materials (provided by the crystallite size variation rate) and those from the comminution process (the rate of change of energy consumed) are enclosed in the pre-exponential factor of the power function in equation (2) (i.e., the crystallite size variation per unit of energy consumed, as calculated for each colorant). The pre-exponential factor is displayed in Fig. 13 as a function of the isothermal bulk modulus for the colorants under investigation.

Incompressibility data in Table 4 perfectly match with the ranking of grindability derived from the crystallite size of colorants under comminution (Fig. 12*a*), and linearly scale with the pre-exponential factor values derived from Equation (2) (Fig. 13). When the bulk modulus is very high (i.e., eskolaite and zircon crystal structures), the material will behave in a brittle way, and the elastic energy supplied during the comminution process will be largely devoted to the creation of lattice defects that provoke the particle breakage (hence, new surface area). On the other hand, if the bulk modulus is lower (i.e., olivine and malayaite crystal structures), much of the supplied elastic energy will be spent for deformation, and the comminution efficiency will drastically decrease.

5. Conclusions

In this work, a detailed inspection of the microstructural evolution of ceramic inks during a micronization process at a pilot plant was carried out. Although no general laws can be stated, some key aspects of the comminution process are identified, highlighting the different mechanisms involved.
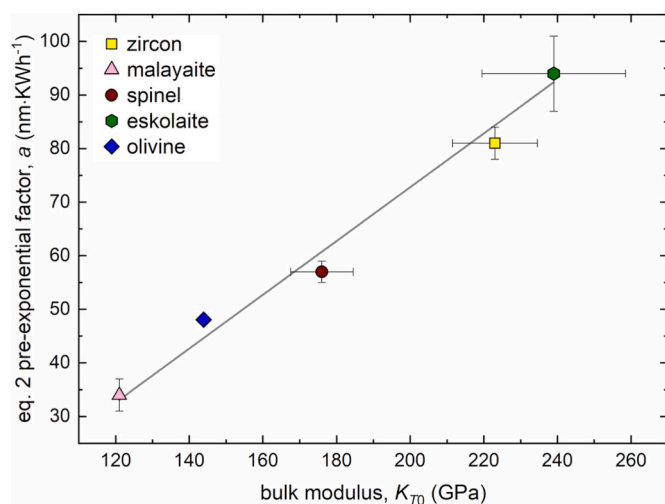
Fig. 13. Pre-exponential factor (a) of the power function $x_{XRD} = a \cdot E_c^b$ as a function of the average isothermal bulk modulus (K_{T0}) for the main phases of the investigated ceramic colorants. Continuous line represents a linear regression of the plotted data.

5.1. Qualitative considerations on energetic consumption-microstructural evolution relation

A linear trend of energy demand with milling can be linked to a microstructural evolution typical of a brittle mechanism. Plastic deformation/particle agglomeration observed in microstructural characterization lead to a reduction of comminution efficiency and an increase in the energy demand. The comminution efficiency, related to the intrinsic properties of the ink is not easily predictable on the base of the physical properties only (Table S1), but the transition between different mechanisms can be suggested (Fig. 14). The energy demand for the particle downsizing of yellow *zrc*, brown *sp*, green *esk*, and blue *ol* colorants scales sublinearly with the milling time. Blue *ol* and pink *mly* require higher energies than *zrc*, *sp*, and *esk* to reach the same micronization degree. The morphology of starting particles, is modified during the comminution process through different breakage mechanisms depending on the crystalline *vs.* amorphous phase content. The predominance of a brittle rather than a plastic regime depends on the specific system. The particles downsizing lower the polydispersity and leads to more and more anhedral particles. Plastic deformation (including particle agglomeration) is particular evident for *mly* and *ol*, where the formation of flake-like particles is observed at every comminution step. On the contrary, fracture deriving from a brittle regime throughout the comminution progress is always observed for *sp* and *esk* samples, and a euhedral to subhedral crystal habit is maintained.

5.2. Effect of milling on crystals properties

The crystalline phase stability depends on the pigment phase composition and properties, and two main aspects are here highlighted:

- A different behavior on comminution can related to the number and relative amount of secondary phases. *Sp* and *zrc* show limited amorphization, mainly related to the main phase depletion. On the other side, unreacted precursors and side products are directly involved in the amorphization degree for *mly* and *ol*. Furthermore, in case of *esk*, the competitive grinding of media milling raises the final amorphous phase content.
- The crystal structure incompressibility (volumetric bulk modulus) of the main crystalline phases perfectly matches with the colorants grindability (ease of micronization), and linearly scale with the pre-exponential term (a) of the power function $x_{XRD} = a \cdot E_c^b$, where the decreasing rate of the crystallite size (x_{XRD}) reduction is function of the increase of consumed energy normalized for the colorant solid load (E_C). The pre-exponential factor of the power function encloses the intrinsic elastic features of materials under micronization and those from the comminution process (the rate of change of energy consumed).

In conclusion, when subjected to a comminution process to produce ultrafine particles, materials characterized by a very high bulk modulus (such as, eskolaite and zircon crystal structures) will convert the kinetic and elastic energy from grinding media mainly to lattice defects creation and provoke particle breakage through brittle fractures. On the contrary, as in the case of olivine and malayaite crystal structures, part of the supplied energy will be converted/dissipated into plastic deformations, drastically decreasing the efficiency of the comminution process. The next studies will be focused on the effect of microstructural changes on the colouring properties in ceramic decoration applications.

Declaration of competing interest

The authors declare that they have no known competing financial interests or personal relationships that could have appeared to influence
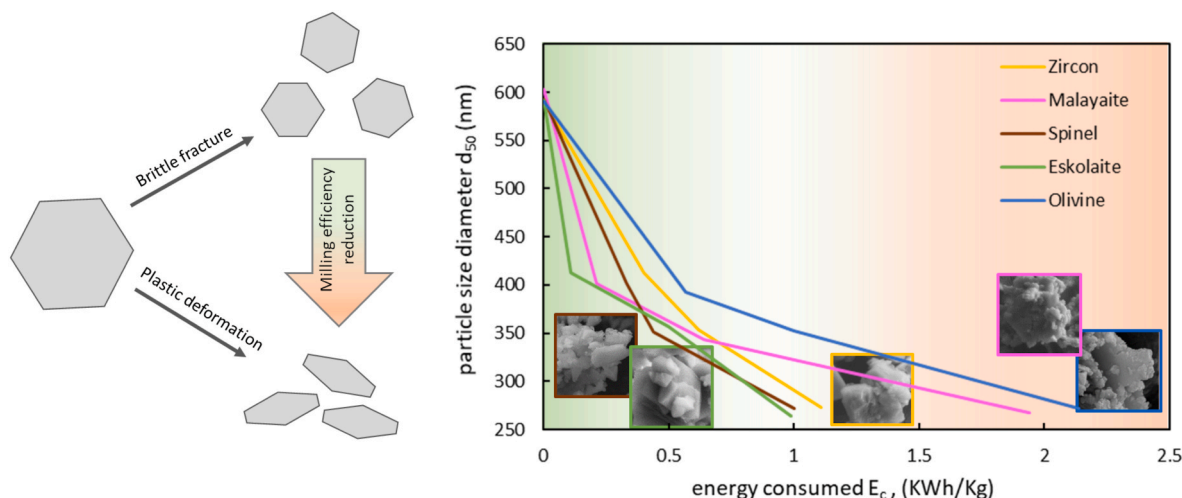

Fig. 14. Effect of milling mechanisms on microstructure and energy consumption trends.

the work reported in this paper.

Appendix A. Supplementary data

Supplementary data to this article can be found online at https://doi.org/10.1016/j.ceramint.2022.09.061.

References

[1] Y. Wang, E. Forssberg, Enhancement of energy efficiency for mechanical production of fine and ultra-fine particles in comminution, China Particuol. 5 (2007) 193–201.

[2] S. Mende, F. Stenger, W. Peukert, J. Schwedes, Mechanical production and stabilization of submicron particles in stirred media mills, Powder Technol. 132 (2003) 64–73.

[3] F. Stenger, S. Mende, J. Schwedes, W. Peukert, Nanomilling in stirred media mills, Chem. Eng. Sci. 60 (2005) 4557–4565.

[4] F. Stenger, S. Mende, J. Schwedes, W. Peukert, The influence of suspension properties on the grinding behavior of alumina particles in the submicron size range in stirred media mills, Powder Technol. 156 (2005) 103–110.

[5] I. Hutchings, Ink-jet printing for the decoration of ceramic tiles: technology and opportunities, In Proc. of XI Congreso Mundial de la Calidad del Azulejo y del Pavimento QUALICER 10 (2010).

[6] C. Molinari, S. Conte, C. Zanelli, M. Ardit, G. Cruciani, M. Dondi, Ceramic pigments and dyes beyond the inkjet revolution: from technological requirements to constraints in colorant design, Ceram. Int. 46 (2020) 21839–21872.

[7] G.L. Güngör, A. Kara, M. Blosi, D. Gardini, G. Guarini, C. Zanelli, M. Dondi, Micronizing ceramic pigments for inkjet printing: Part I. Grindability and particle size distribution, Ceram. Int. 41 (2015) 6498–6506.

[8] C. Zanelli, G.L. Güngör, A. Kara, M. Blosi, D. Gardini, G. Guarini, M. Dondi, Micronizing ceramic pigments for inkjet printing: Part II. Effect on phase composition and color, Ceram. Int. 41 (2015) 6507–6517.

[9] J.H. Lee, K.S. Han, H.J. Hwang, J.W. Kwon, J.H. Kim, K.T. Hwang, Effects of micronization on optical property of ceramic pigments for digital ink-jet printing, J. Ceram. Process. Res. 20 (2019) 127–132.

[10] H. Yüngevis, E. Ozel, Effect of the milling process on the properties of $CoFe_2O_4$ pigment, Ceram. Int. 39 (2013) 5503–5511.

[11] Y. Wang, Q. Wang, Q. Chang, S. Hu, X. Wang, K. Yang, Effect of particle size on the blue chromate pigment $CoAl_2O_4$, J. Ceram. Sci. Technol. 9 (2018) 43–46.

[12] D. Guo, Q. Yang, P. Chen, Y. Chu, Y. Zhang, P. Rao, The influence of micronization on the properties of $Pr-ZrSiO_4$ pigment, Dyes Pigments 153 (2018) 74–83.

[13] H. Liu, Q. Wang, Q. Chang, C. Wang, Y. Wang, Y. Wang, X. Zhang, Relationship between the colour and particle size of the ultrafine $V-ZrSiO_4$ and $Pr-ZrSiO_4$ pigments and their mixture, Mater. Res. Express 6 (2019) 075214.

[14] A. Kwade, Wet comminution in stirred media mills — research and its practical application, Powder Technol. 105 (1999) 14–20.

[15] A. Kwade, J. Schwedes, Breaking characteristics of different materials and their effect on stress intensity and stress number in stirred media mills, Powder Technol. 122 (2002) 109–121.

[16] W. Peukert, Material properties in fine grinding, Int. J. Miner. Process. 74 (2004) S3–S17.

[17] C. Knieke, M. Sommer, W. Peukert, Identifying the apparent and true grinding limit, Powder Technol. 195 (2009) 25–30.

[18] C. Knieke, C. Steinborn, S. Romeis, W. Peukert, S. Breitung-Faes, A. Kwade, Nanoparticle production with stirred-media mills: opportunities and limits, Chem. Eng. Technol. 33 (2010) 1401–1411.

[19] C. Knieke, S. Romeis, W. Peukert, Influence of process parameters on breakage kinetics and grinding limit at the nanoscale, AIChE J. 57 (2011) 1751–1758.

[20] C. Suryanarayana, Mechanical alloying and milling, Prog. Mater. Sci. 46 (2001) 1–184.

[21] M. Wang, H. Sun, B. Pang, X. Xi, Z. Nie, Structure evolution of Y_2O_3 and consequent effects on mechanical properties of $W-Y_2O_3$ alloy prepared by ball milling and SPS, Mater. Sci. Eng., A 832 (2022), 142448.

[22] R.L. Snyder, D.L. Bish, Quantitative analysis, in: R.L. Snyder, D.L. Bish (Eds.), Modern Powder Diffraction, De Gruyter, Berlin, 1989, pp. 101–144.

[23] A.F. Gualtieri, V. Riva, A. Bresciani, S. Maretti, M. Tamburini, A. Viani, Accuracy in quantitative phase analysis of mixtures with large amorphous contents. The case of stoneware ceramics and bricks, J. Appl. Crystallogr. 47 (2014) 835–846.

[24] M. Dondi, R.A. Eppler, Ceramic colorant, in: Ullmann's Encyclopedia of Industrial Chemistry, John Wiley & Sons, 2000, pp. 1–18.

[25] M. Ardit, G. Cruciani, F. Di Benedetto, L. Sorace, M. Dondi, New spectroscopic and diffraction data to solve the vanadium-doped zircon pigment conundrum, J. Eur. Ceram. Soc. 38 (2018) 5234–5245.

[26] H. Zhang, B. Hengzhong, J.F. Banfield, The size dependence of the surface free energy of titania nanocrystals, Phys. Chem. Chem. Phys. 11 (2009) 2553–2558.

[27] E.J. Mittemeijer, P. Scardi, Diffraction Analysis of the Microstructure of Materials, vol. 68, Springer Science & Business Media, 2013.

[28] V.G. Gryaznov, I.A. Polonsky, A.E. Romanov, L.I. Trusov, Size effects of dislocation stability in nanocrystals, Phys. Rev. B 44 (1991) 42.

[29] D.L. Anderson, Theory of the Earth, Blackwell Scientific Publications, 1989.

[30] R.J. Angel, Equatioms of state, Rev. Mineral. Geochem. 41 (2000) 35–59.

[31] Y. Sato, S.I. Akimoto, Hydrostatic compression of four corundum-type compounds: α-Al_2O_3, V_2O_3, Cr_2O_3, and α-Fe_2O_3, J. Appl. Phys. 50 (1979) 5285–5291.

[32] L.W. Finger, R.M. Hazen, Crystal structure and isothermal compression of Fe_2O_3, Cr_2O_3, and V_2O_3 to 50 kbars, J. Appl. Phys. 51 (1980) 5362–5367.

[33] S. Rekhi, L.S. Dubrovinsky, R. Ahuja, S.K. Saxena, B. Johansson, Experimental and theoretical investigations on eskolaite (Cr_2O_3) at high pressures, J. Alloys Compd. 302 (2000) 16–20.

[34] J. Mougin, T. Le Bihan, G. Lucazeau, High-pressure study of Cr_2O_3 obtained by high-temperature oxidation by X-ray diffraction and Raman spectroscopy, J. Phys. Chem. Solid. 62 (2001) 553–563.

[35] P. Dera, B. Lavina, Y. Meng, V.B. Prakapenka, Structural and electronic evolution of Cr_2O_3 on compression to 55 GPa, J. Solid State Chem. 184 (2011) 3040–3049.

[36] A. Kantor, I. Kantor, M. Merlini, K. Glazyrin, C. Prescher, M. Hanfland, L. Dubrovinsky, High-pressure structural studies of eskolaite by means of single-crystal X-ray diffraction, Am. Mineral. 97 (2012) 1764–1770.

[37] H. Özkan, L. Cartz, J.C. Jamieson, Elastic constants of nonmetamict zirconium silicate, J. Appl. Phys. 45 (1974) 556–562.

[38] H. Özkan, J.C. Jamieson, Pressure dependence of the elastic constants of nonmetamict zircon, Phys. Chem. Miner. 2 (1978) 215–224.

[39] R.M. Hazen, L.W. Finger, Crystal structure and compressibility of zircon at high pressure, Am. Mineral. 64 (1979) 196–201.

[40] S. Ríos, T. Boffa-Ballaran, Microstructure of radiation-damaged zircon under pressure, J. Appl. Crystallogr. 36 (2003) 1006–1012.

[41] S. Ono, Y. Tange, I. Katayama, T. Kikegawa, Equations of state of $ZrSiO_4$ phases in the upper mantle, Am. Mineral. 89 (2004) 185–188.

[42] H. Özkan, Correlations of the temperature and pressure dependencies of the elastic constants of zircon, J. Eur. Ceram. Soc. 28 (2008) 3091–3095.

[43] D. Levy, A. Pavese, M. Hanfland, Phase transition of synthetic zinc ferrite spinel ($ZnFe_2O_4$) at high pressure, from synchrotron X-ray powder diffraction, Phys. Chem. Miner. 27 (2000) 638–644.

[44] D. Levy, V. Diella, A. Pavese, M. Dapiaggi, A. Sani, P-V equation of State, thermal expansion, and P-T stability of synthetic zincochromite ($ZnCr_2O_4$ spinel), Am. Mineral. 90 (2005) 1157–1162.

[45] Y. Liu, J. Xing, Y. Li, J. Tan, L. Sun, J. Yan, Mechanical properties and anisotropy of thermal conductivity of $Fe_{3-x}Cr_xO_4$ ($x= 0–3$), J. Mater. Res. 31 (2016) 3805–3813.

[46] L. Zhang, Single crystal hydrostatic compression of $(Mg,Mn,Fe,Co)_2SiO_4$ olivines, Phys. Chem. Miner. 25 (1998) 308–312.

[47] S. Rath, M. Kunz, R. Miletich, Pressure-induced phase transition in malayaite, $CaSnOSiO_4$, Am. Mineral. 88 (2003) 293–300.